

ARMY RESEARCH LABORATORY



## **Materials Research of Perovskite Thin Films for Uncooled Infrared (IR) Detectors**

**by Wendy L. Sarney, Kimberley A. Olver, John W. Little,  
Frank E. Livingston, Krisztian Niesz, and Daniel E. Morse**

ARL-TR-5600

July 2011

## **NOTICES**

### **Disclaimers**

The findings in this report are not to be construed as an official Department of the Army position unless so designated by other authorized documents.

Citation of manufacturer's or trade names does not constitute an official endorsement or approval of the use thereof.

Destroy this report when it is no longer needed. Do not return it to the originator.

# **Army Research Laboratory**

Adelphi, MD 20783-1197

---

**ARL-TR-5600**

**July 2011**

---

## **Materials Research of Perovskite Thin Films for Uncooled Infrared (IR) Detectors**

**Wendy L. Sarney, Kimberley A. Olver, and John W. Little,  
Sensors and Electron Devices Directorate, ARL**

**Frank E. Livingston  
The Aerospace Corporation**

**Krisztian Niesz and Daniel E. Morse  
Institute for Collaborative Biotechnologies  
University of California Santa Barbara**

# REPORT DOCUMENTATION PAGE

Form Approved  
OMB No. 0704-0188

Public reporting burden for this collection of information is estimated to average 1 hour per response, including the time for reviewing instructions, searching existing data sources, gathering and maintaining the data needed, and completing and reviewing the collection information. Send comments regarding this burden estimate or any other aspect of this collection of information, including suggestions for reducing the burden, to Department of Defense, Washington Headquarters Services, Directorate for Information Operations and Reports (0704-0188), 1215 Jefferson Davis Highway, Suite 1204, Arlington, VA 22202-4302. Respondents should be aware that notwithstanding any other provision of law, no person shall be subject to any penalty for failing to comply with a collection of information if it does not display a currently valid OMB control number.

**PLEASE DO NOT RETURN YOUR FORM TO THE ABOVE ADDRESS.**

1. REPORT DATE (DD-MM-YYYY)	2. REPORT TYPE	3. DATES COVERED (From - To)			
July 2011	Progress	August 2009 to January 2010			
4. TITLE AND SUBTITLE		5a. CONTRACT NUMBER			
Materials Research of Perovskite Thin Films for Uncooled Infrared (IR) Detectors		5b. GRANT NUMBER			
6. AUTHOR(S)		5c. PROGRAM ELEMENT NUMBER			
Wendy L. Sarney, Kimberley A. Olver, John W. Little, Frank E. Livingston, Krisztian Niesz, and Daniel E. Morse		5d. PROJECT NUMBER			
7. PERFORMING ORGANIZATION NAME(S) AND ADDRESS(ES)		5e. TASK NUMBER			
U.S. Army Research Laboratory ATTN: RDRL-SEE-I 2800 Powder Mill Road Adelphi, MD 20783-1197		5f. WORK UNIT NUMBER			
9. SPONSORING/MONITORING AGENCY NAME(S) AND ADDRESS(ES)		8. PERFORMING ORGANIZATION REPORT NUMBER			
Army Research Office – Dr. Robert Kokoska ATTN: RDRL-ROP P.O. Box 12211 Research Triangle Park, NC 27709-2211		ARL-TR-5600			
10. SPONSOR/MONITOR'S ACRONYM(S)		11. SPONSOR/MONITOR'S REPORT NUMBER(S)			
12. DISTRIBUTION/AVAILABILITY STATEMENT Approved for public release; distribution unlimited.					
13. SUPPLEMENTARY NOTES					
14. ABSTRACT This report describes the highlights and summary of the year two, quarters two and three progress for the 6.2 project "Improved Sensitivity Low-Cost Uncooled IR Detector Focal-Plane Arrays." This work occurred during the August 2009–January 2010 time period. The program goals for year 2-quarters 2&3 corresponded to the continued expansion of our BaTiO <sub>3</sub> nanomaterial synthesis capabilities and deposition methods, laser-induced pyroelectric phase conversion studies and nanoscale characterization of the pyroelectric activation process, and fabrication of IR test heterostructures for pyroelectrical analysis, along with the development of a technique for generating the requisite IR absorbing layer.					
15. SUBJECT TERMS Laser processing, perovskites, uncooled infrared					
16. SECURITY CLASSIFICATION OF:		17. LIMITATION OF ABSTRACT	18. NUMBER OF PAGES	19a. NAME OF RESPONSIBLE PERSON Wendy L. Sarney	
a. REPORT Unclassified	b. ABSTRACT Unclassified	c. THIS PAGE Unclassified	UU	34	19b. TELEPHONE NUMBER (Include area code) (301) 394-5761

---

## Contents

---

<b>List of Figures</b>	<b>iv</b>
<b>List of Tables</b>	<b>v</b>
<b>Acknowledgments</b>	<b>vi</b>
<b>1. Introduction</b>	<b>1</b>
<b>2. Progress by The Aerospace Corporation (Aerospace)</b>	<b>2</b>
2.1 Influence of Perovskite Film Thickness on Optical Band Gap Energy .....	2
2.2 Enhancements to the Laser-scripted Pulse Modulation Setup .....	5
2.3 Digitally-scripted Laser Genotype Direct-write Processing – Continued Success! .....	7
<b>3. Progress by the Institute for Collaborative Biotechnologies (ICB)</b>	<b>12</b>
3.1 Tc with $Ba_{1-x}Sr_xTiO_3$ ; Doping with $CeO_2$ ; Preparation of Thicker Films.....	12
3.2 Further Progress in Scale-Up and Delivery to Quallion.....	16
<b>4. Progress by the Army Research Laboratory (ARL)</b>	<b>17</b>
4.1 Sacrificial Layer Deposition; Electrical Characterization; Nanostructured IR Absorbing Layer Development .....	17
4.1.1 Sacrificial Layer Deposition.....	17
4.1.2 Electrical Characterization .....	18
4.1.3 Nanostructured IR Absorbing Layer Development.....	18
4.2 Update of Proposed Processing Steps .....	19
<b>5. Plans and Goals for Year 2 Quarter 4</b>	<b>20</b>
<b>6. Metrics for Year 2 Quarters 2 and 3</b>	<b>21</b>
6.1 Publications .....	21
6.2 Conferences and Symposia .....	21
<b>7. References</b>	<b>23</b>
<b>List of Symbols, Abbreviations, and Acronyms</b>	<b>24</b>
<b>Distribution List</b>	<b>25</b>

---

## List of Figures

---

Figure 1. Project schedule for year 2 .....	1
Figure 2. (a) Optical transmission spectra measured for BaTiO <sub>3</sub> films with varying thickness. (b) First-derivative plots of the transmission spectra that were used to determine that band gap energies (E <sub>g</sub> ) as a function of film thickness.....	3
Figure 3. Compilation of band gap energies for BaTiO <sub>3</sub> as a function of film thickness, where E <sub>g</sub> values have been derived from literature sources (red) and compared with the E <sub>g</sub> values measured for the ICB films (blue). The solid lines represent linear fits to the data, and are intended as a visual aid. The corresponding energies of the laser processing wavelengths ( $\lambda=266$ nm and $\lambda=355$ nm) are also shown (grey) for comparison. ....	4
Figure 4. Photographic images of the laser genotype pulse modulation optical beam lines (left) and the new dual-beam SHG spectroscopic detection system (right) for phase conversion analysis during static exposures and dynamic raster patterning.....	6
Figure 5. Raman spectra measured for BaTiO <sub>3</sub> thin-films following conventional laser direct-write processing at $\lambda=266$ nm and 5 kHz.....	8
Figure 6. SEM images of BaTiO <sub>3</sub> thin-films that were acquired (a) prior to laser exposure and (b)–(d) following conventional laser direct-write processing at $\lambda=266$ nm. ....	9
Figure 7. Raman spectra measured for BaTiO <sub>3</sub> thin-films following digitally-scripted laser genotype direct-write processing at $\lambda=266$ nm and 5 kHz. The laser pulse scripts corresponded to the following parameters: <i>script 1</i> , 90 pulses, $1.5\text{ J}\cdot\text{cm}^{-2}$ ; <i>script 2</i> , 180 pulses, $1.6\text{ J}\cdot\text{cm}^{-2}$ ; <i>script 3</i> , 240 pulses, $3.1\text{ J}\cdot\text{cm}^{-2}$ (max).....	11
Figure 8. AFM images of BaTiO <sub>3</sub> thin-films that were acquired (a) prior to laser exposure and (b) following digitally-scripted laser genotype direct-write processing and pyroelectric phase conversion at $\lambda=355$ nm. Note that the perovskite film remains unperturbed during the laser-induced phase transformation process when laser pulse “scripting” is employed for high fidelity heat control. ....	12
Figure 9. TEM and XRD analyses of BSTO nanoparticles prepared by vapor diffusion catalytic synthesis. Dotted lines on the XRD curve show the positions of the (110) reflections in pure bulk BaTiO <sub>3</sub> and SrTiO <sub>3</sub> , respectively.....	13
Figure 10. PTCR (positive thermal coefficient of resistivity) of the sintered BSTO ceramic, showing a reduced Curie temperature of ca. 80 °C. ....	14
Figure 11. TEM image of CeO <sub>2</sub> nanoparticles prepared by vapor diffusion catalytic synthesis.....	14
Figure 12. SEM images of the high-quality doped BSTO films produced by layer-by-layer deposition followed by annealing. ....	15
Figure 13. IR test heterostructure.....	17
Figure 14. Wire bonding for capacitance measurements.....	18
Figure 15. Processing steps required for the generation of nanostructured Si pillars for enhanced IR absorption.....	19

Figure 16. AFM images of Au particle formation prior to etching. ....	19
Figure 17. Pixel formation accomplished via conventional approaches.....	20
Figure 18. Pixel formation accomplished via laser-induced pyroelectric activation.....	20

---

## **List of Tables**

---

Table 1. Operational characteristics of the laser system integrated into the laser genotype direct-write processing setup. ....	6
---	---

---

## Acknowledgments

---

We acknowledge support by the Institute for Collaborative Biotechnologies through grant DAAD19-03-D-0004 from the U.S. Army Research Office and The Aerospace Corporation Independent Research and Development (IR&D) Program and the Product and Development (PDP) Program.

## 1. Introduction

This report describes the highlights and summary of the year two, quarters two and three (Y2Q2/3) progress for the 6.2 project “Improved Sensitivity Low-Cost Uncooled IR Detector Focal-Plane Arrays.” This work occurred during the August 2009–January 2010 time period. The project schedule for year 2 is summarized in figure 1. A description of the background technical information and earlier progress is discussed in prior technical reports (1–4).

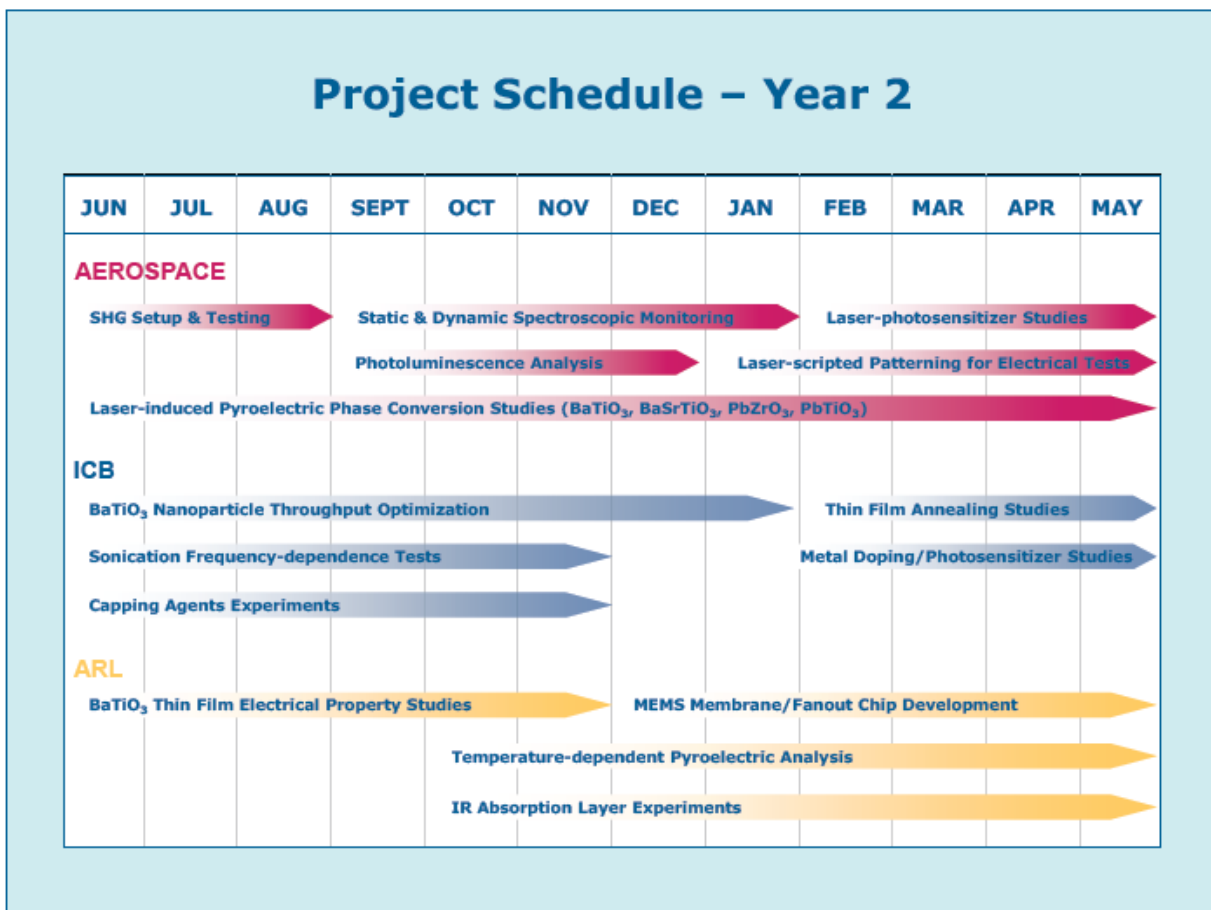


Figure 1. Project schedule for year 2.

The program goals for year 2-quarters 2&3 corresponded to the continued expansion of our  $\text{BaTiO}_3$  nanomaterial synthesis capabilities and deposition methods, laser-induced pyroelectric phase conversion studies and nanoscale characterization of the pyroelectric activation process, and fabrication of IR test heterostructures for pyroelectrical analysis, along with the development of a technique for generating the requisite IR absorbing layer. Respective team highlights include:

*Aerospace*: Investigated the optical transmission properties of functionalized BaTiO<sub>3</sub> nanoparticle films as a function of film thickness, which will help to optimize the laser-induced pyroelectric phase conversion process. We continued investigations into the laser-induced pyroelectric cubic-tetragonal phase conversion of functionalized BaTiO<sub>3</sub> nanoparticle thin-films at multiple UV wavelengths – including *laser-scripted* modulation at =355 nm and *intensity modulation* and *variable exposure* at =266 nm. Efforts also focused on the development and implementation of piezoresponse force microscopy (PFM) techniques for nanoscale characterization of the laser-induced pyroelectric phase activation. We further expanded the capabilities and versatility of the laser-scripted processing and spectroscopic detection schemes to include a broader range of processing wavelengths, pulse durations, and pulse repetition rates.

*ICB*: Extended the bio-inspired vapor diffusion catalytic synthesis methods to include the growth and deposition of functionalized, high purity barium strontium titanate (Ba<sub>1-x</sub>Sr<sub>x</sub>TiO<sub>3</sub>, BSTO) nanoparticle thin-films, where the Ba/Sr composition can be altered to precisely tune the electric properties of the ceramic films. Doping of the BSTO nanoparticles with CeO<sub>2</sub> has also been accomplished, which will enhance UV absorption in the native films and improve the laser-induced phase conversion efficiency. Further progress regarding scale-up and sonication-accelerated synthesis was achieved, along with the improved methods for the deposition of thick micrometer-scale BSTO.

*ARL*: Investigated the implementation of potential release (sacrificial) layers for the formation of the requisite suspended perovskite MEMS membranes, including polymethyl methacrylate (PMMA) and other standard photoresists. Continued and expanded the development of the IR test heterostructure, which included electrical characterization, fabrication of nanostructured Si layers for enhanced IR absorption, and improvements in the proposed detector pixel processing protocol.

All project teams have accomplished their respective planned milestones for Y2Q2/3 with distinction, and highlights of the major activities are provided in the subsequent sections of this report.

---

## **2. Progress by The Aerospace Corporation (Aerospace)**

---

### **2.1 Influence of Perovskite Film Thickness on Optical Band Gap Energy**

Our second and third quarter efforts for year 2 have focused on the influence of film thickness and morphology on the inherent band gap energies of the BaTiO<sub>3</sub> nanostructured films, which will affect the laser-material coupling efficiency as well as the extent of pyroelectric phase conversion. Figure 2a shows the optical transmission spectra that were measured for BaTiO<sub>3</sub> films as a function of film thickness, where the film thickness ranged from ca. 200 nm to 5  $\mu$ m and the optical spectra have been corrected for reflection and scattering and thus represent the

pure transmission characteristics of the nascent film. The BaTiO<sub>3</sub> nanoparticles were deposited on 1 mm thick optical quality quartz substrates at room temperature and ambient pressure. For films with a thickness <500 nm, the BaTiO<sub>3</sub> nanoparticles were pre-functionalized with oleic acid and dispersed in a hexane colloidal solution for eventual layer-by-layer spin coating. For films with a thickness >500 nm, the BaTiO<sub>3</sub> films were cast as nanoparticle suspensions in methanol/butanol, and then dried in a vacuum desiccator for 48 hr.

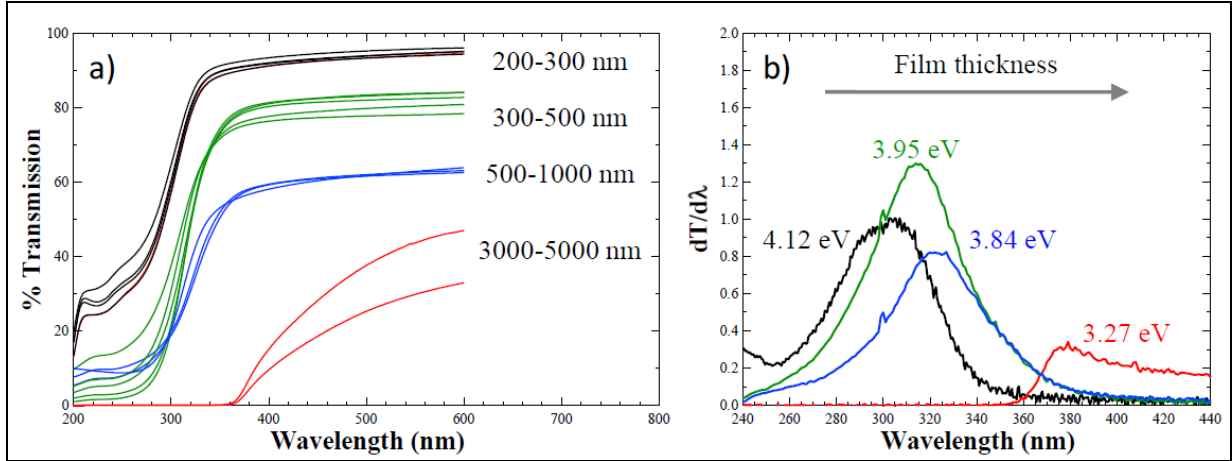


Figure 2. (a) Optical transmission spectra measured for BaTiO<sub>3</sub> films with varying thickness. (b) First-derivative plots of the transmission spectra that were used to determine that band gap energies ( $E_g$ ) as a function of film thickness.

The spectra shown in figure 2a reveal high transparency in the visible and near-IR regions particularly for the BaTiO<sub>3</sub> films with thicknesses <1  $\mu\text{m}$  – and suggest only a small degree of local surface roughness and good film homogeneity. The thinner films display higher transparency and retain higher homogeneity and less roughness; these characteristics have been confirmed with complementary analysis using contact profilometry, scanning electron microscope (SEM) and atomic force microscopy (AFM) techniques. For the thicker micron-sized films (>1  $\mu\text{m}$ ), inter-band transitions occur at wavelengths of  $\lambda < 450\text{--}500$  nm, and the transmission falls rapidly to less than 10% at wavelengths of  $\lambda < 400$  nm. In contrast, inter-band transitions occur at wavelengths of  $\lambda < 300$  nm for the thinner 200–500 nm-thick films, and the 10% cut-off occurs at UV wavelengths of <260 nm.

Figure 2b displays the corresponding first-derivative plots of the optical transmission spectra as a function of BaTiO<sub>3</sub> film thickness. The band gap energies were estimated from the peak maxima positions, and the results presented in figure 2b reveal that the band gap energies for BaTiO<sub>3</sub> exhibit a strong dependence on film thickness. The calculated band gap energies displayed the following trend with film thicknesses denoted in parentheses:  $E=3.27\pm0.4$  eV (3–5  $\mu\text{m}$ ),  $3.84\pm0.2$  eV (0.5–1  $\mu\text{m}$ ),  $3.95\pm0.1$  eV (300–500 nm), and  $4.12\pm0.05$  eV (200–300 nm). Our results also reveal that the fluctuations in the band gap energies that were observed previously

with thicker and unfunctionalized  $\text{BaTiO}_3$  nanoparticle films have been notably reduced, and laser light scattering has been decreased as well.

While the band gap energy fluctuations have been reduced, the *absolute* band gap energies for the thinner and functionalized  $\text{BaTiO}_3$  films are appreciably *blue-shifted* compared with the thicker micrometer-scale films. Figure 3 summarizes the band gap energies as a function of  $\text{BaTiO}_3$  film thickness, where the band gap values have been derived from a survey of the relevant literature and from the composite ICB sample sets. The literature data encompass a diverse array of  $\text{BaTiO}_3$  synthesis and deposition methods, including melt-grown single crystals (5), pulsed laser deposition (PLD) (6), sol-gel (7–9), spray pyrolysis (10), and molecular beam epitaxy (MBE) (11). Clearly, the band gap energies can be influenced by factors other than film thickness – such as synthesis and deposition method, extent of crystallinity and crystallite grain size, and intrinsic and extrinsic stresses (defects, lattice mismatch). However, when applying a specific protocol for particle synthesis and thin-film preparation, the band gap energies are highly consistent and appear to correlate quite well with the  $\text{BaTiO}_3$  film thickness.

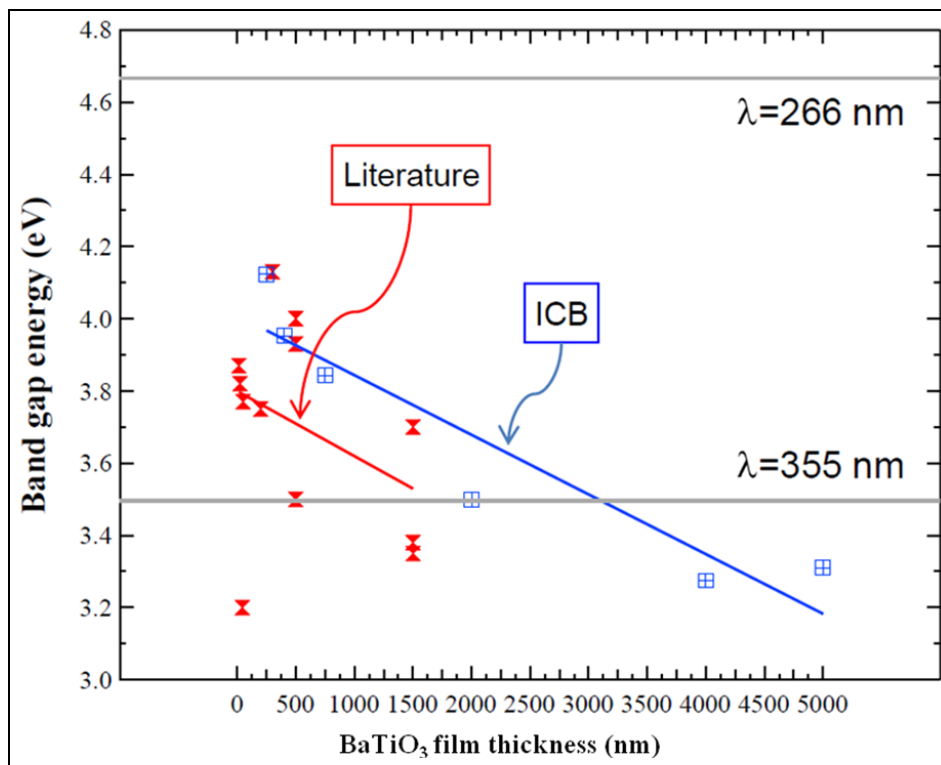


Figure 3. Compilation of band gap energies for  $\text{BaTiO}_3$  as a function of film thickness, where  $E_g$  values have been derived from literature sources (red) and compared with the  $E_g$  values measured for the ICB films (blue). The solid lines represent linear fits to the data, and are intended as a visual aid. The corresponding energies of the laser processing wavelengths ( $\lambda = 266 \text{ nm}$  and  $\lambda = 355 \text{ nm}$ ) are also shown (grey) for comparison.

This film-thickness dependent behavior of the band gap energy will severely impact the selection of the appropriate laser processing wavelengths and other laser parameters that are requisites for effective laser energy coupling and optimal pyroelectric phase transformation. The extent to which the band gap energy determines the laser-material coupling and phase state selection efficiency is related to the mechanisms and energy dependence of the laser-induced phase conversion process; we are currently exploring the photon dependence of the pyroelectric cubic-to-tetragonal phase conversion in BaTiO<sub>3</sub> thin-films at multiple UV laser wavelengths in order to optimize pyroelectric activation.

Laser processing at  $\lambda=355$  nm permits phase control in thick micrometer-scale BaTiO<sub>3</sub> films due to the enhanced optical penetration depth, but requires higher incident laser energies for phase conversion due to the reduced absorption. The photon flux at  $=355$  nm must be carefully modulated to preclude damage to the underlying adhesion and electrical contact layers. Conversely, laser processing at  $\lambda=266$  nm facilitates access to a much wider range of film thicknesses with enhanced energy absorption, smaller optical penetration depth, and thus higher localized energy density. However, this increase in energy absorption leads to a smaller laser processing window and requires exquisite laser pulse script control and per-pulse intensity modulation.

## 2.2 Enhancements to the Laser-scripted Pulse Modulation Setup

The optical results presented in figures 2 and 3 strongly support the notion that the laser processing method must be highly versatile and adaptable, and facilitate phase conversion over a wide range of laser wavelengths, pulse durations and repetition rates. Figure 4 displays photographic images of the various optical beam lines that comprise the laser-scripted genotype pulse modulation system (*left panel*) and spectroscopic pump-probe detection scheme (*right panel*). The laser genotype processing setup now retains four separate optical beam lines, where each beam lines includes the appropriate polarizers, waveplates, focusing and collimation lenses, and electro-optic Pockels cell modulators and amplifier assemblies that are required for position-synchronized and laser-scripted direct-write processing. The revised laser pulse modulation setup also includes four laser systems that span a broad range of laser processing parameters and capabilities. With adaptations to our current laser systems and optical configurations, we can examine laser phase conversion under a wide range of wavelengths (250–1100 nm), along with variations in pulse length (100 fs–5 ns) and pulse repetition rate conditions (5 kHz–80 MHz). The specifications for the integrated laser systems are comprehensively summarized in table 1.

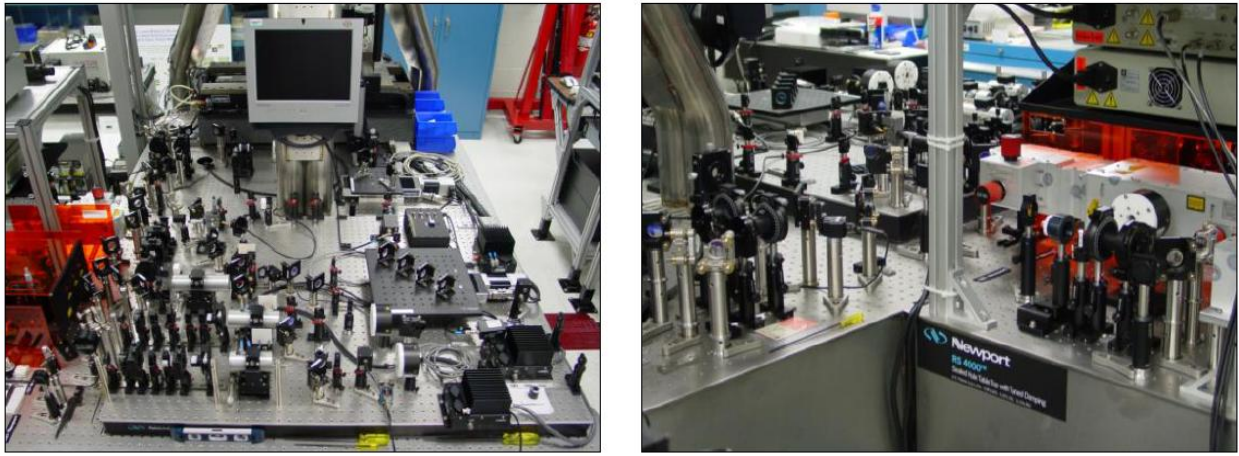


Figure 4. Photographic images of the laser genotype pulse modulation optical beam lines (*left*) and the new dual-beam SHG spectroscopic detection system (*right*) for phase conversion analysis during static exposures and dynamic raster patterning.

Table 1. Operational characteristics of the laser system integrated into the laser genotype direct-write processing setup.

<i>Laser system</i>	<i>Operational parameters</i>			
	<i>wavelength</i>	<i>rep. rate</i>	<i>pulse width</i>	<i>power</i>
diode-pumped, mode-locked Ti:sapphire (Spectra-Physics, MaiTai)	750–920 nm	80 MHz	100 fs	1 W
diode-pumped, Q-switched intra-cavity doubled Nd:YLF (Spectra-Physics Evolution-30)	527 nm	5 kHz	300 ns	30 W
Ti:sapphire regenerative amplifier with pulse stretcher/compressor (Spectra-Physics Spitfire)	750–920 nm	5 kHz	100–500 fs	2.5 W
diode-pumped, mode-locked Nd:YVO <sub>4</sub> laser with SESAM (Spectra-Physics Vanguard)	1064 nm 355/532 nm	80 MHz	2 ps	4 W 1 W
diode-pumped, mode-locked Nd:YVO <sub>4</sub> (Spectra-Physics BL6 series)	1064 nm	10–50 kHz	6 ns	4–7 W

Our recent efforts in year 2 have also focused on the continued development and implementation of a spectroscopic detection scheme for end-point analysis of the laser-induced pyroelectric activation and phase conversion process, where we have now constructed and tested the dual-beam second harmonic generation (SHG) and photoemission setup. The dual-beam SHG spectroscopic detection scheme permits the simultaneous delivery of the UV laser processing beam and IR SHG pump-beam to a substrate under *dynamic patterning conditions* and *static exposure conditions*; these modifications will help facilitate laser pulse script optimization and refinement via SHG and photoluminescence measurements, along with improving process and quality control. The IR probe beam is fiber-coupled to the substrate surface and also feeds into the static exposure beam line.

### 2.3 Digitally-scripted Laser Genotype Direct-write Processing – Continued Success!

We have continued to investigate the capability of using multi-wavelength laser-scripted direct-write processing techniques to induce site-selective and patterned micro- and nano-scale transformation of BaTiO<sub>3</sub> nanoparticle aggregates from the nascent pyroelectrically-inactive *cubic* phase to the pyroelectrically-active *tetragonal* phase. Recall that our intent is to use laser irradiation to achieve in-band excitation of the BaTiO<sub>3</sub> crystal, where the resonant irradiation energy is above or very close to the band gap of BaTiO<sub>3</sub>, and will lead to the excitation of valence electrons and the formation of excited electronic states. The exchange of energy between the electronic excited states and lattice vibrational energy will lead to a rapid temperature rise in the crystal lattice (i.e., electron-lattice coupling) and a concomitant cubic-to-tetragonal phase transition.

Our recent research efforts have focused on the implementation of deep-UV laser processing at  $\lambda=266$  nm for pyroelectric phase activation. Like our prior experimental investigations using  $\lambda=355$  nm irradiation, two distinct laser processing approaches were employed to examine laser-mediated pyroelectric phase conversion in the bio-inspired BaTiO<sub>3</sub> thin-films at  $\lambda=266$  nm: conventional laser direct-write processing and genotype-inspired, digitally-scripted laser processing. Again, the contrasting results from these two approaches clearly illustrate the importance of synchronized, high fidelity photon modulation during laser patterning for optimal phase conversion. In the conventional laser direct-write processing scenario, the incident and repetitive laser pulse train remains un-articulated, and the only modulation employed corresponds to simple power control, i.e., the laser pulse intensities are uniformly attenuated to achieve the desired static power level and per-pulse fluence for material exposure and processing.

Figure 5 provides a compilation of the Raman spectra that were measured for a set of 200–300 nm-thick BaTiO<sub>3</sub> thin-films following conventional laser direct-write processing at  $\lambda=266$  nm. The vertical lines denote the locations of the prominent Raman-active bands associated with the tetragonal phase of BaTiO<sub>3</sub>, which occur at 305 cm<sup>-1</sup>, 540 cm<sup>-1</sup>, and 720 cm<sup>-1</sup>. The cubic-to-tetragonal phase conversion was examined over a wide laser parameter space, including power and per pulse intensity (conversion threshold), pulse repetition rate (thermal diffusion and heat capacity), pulse length (conversion kinetics), and total exposure dose (sequential phase conversion). The variation in laser pulse repetition rate will help to illuminate the kinetics of energy transfer into the BaTiO<sub>3</sub> crystal lattice system. Additionally, the variation in pulse length will assist in determining whether partial or complete phase conversion can be accomplished during a single pulse event (intra-pulse) or by the administration of a succession of laser pulses (inter-pulse).

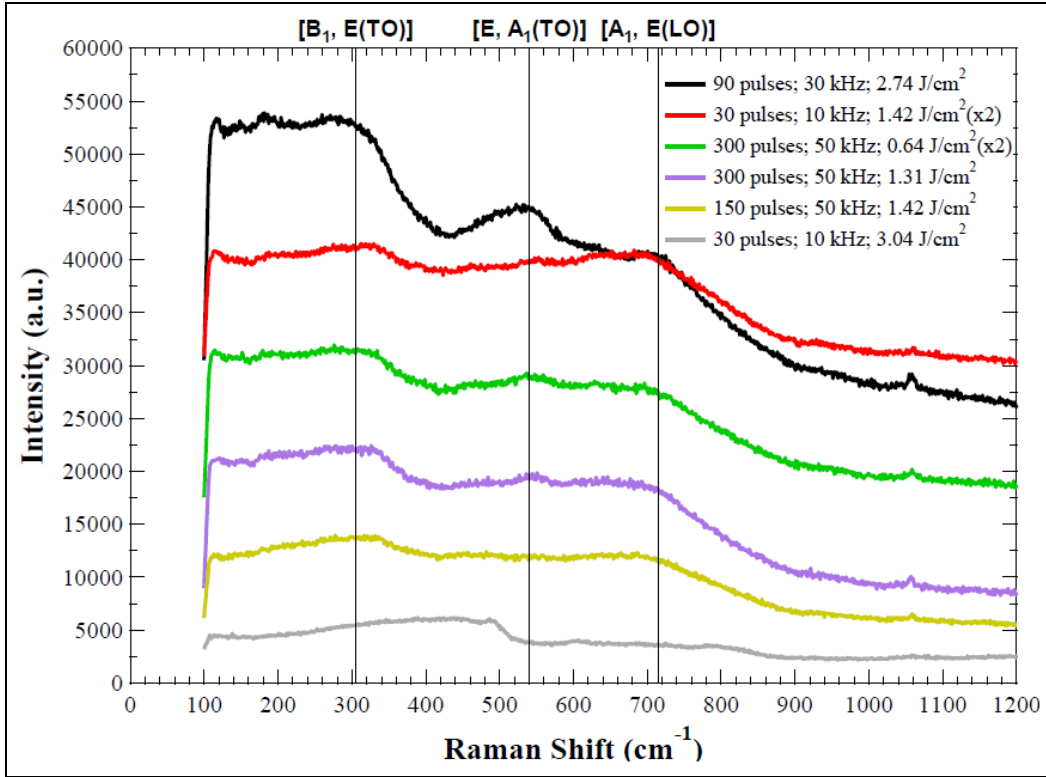


Figure 5. Raman spectra measured for BaTiO<sub>3</sub> thin-films following conventional laser direct-write processing at  $\lambda=266$  nm and 5 kHz.

Despite the increased absorption at  $\lambda=266$  nm – where the absorptivity of the ultra thin BaTiO<sub>3</sub> films is ca. 60% compared to only ca. 10% at  $\lambda=355$  nm – appreciable phase transformation was not detected, but instead was accompanied by significant film disruption and desorption. For these conventional laser processing experiments, the *average* number of pulses delivered to each laser spot ranged from 30 to 300 pulses, the repetition rates were varied from 10 kHz to 50 kHz, and the per-pulse fluence ranged from  $0.64\text{ J}\cdot\text{cm}^{-2}$  to  $3.04\text{ J}\cdot\text{cm}^{-2}$ . The lower power and higher pulse repetition rate exposures yielded little change in the Raman spectra, and indicate that the pulse energies and related thermal transients were insufficient to induce phase conversion. The higher power and lower pulse repetition rate exposures also show no evidence of structural phase conversion, but did reveal appreciable film fracture and material desorption due to excessive heat loading and thermal confinement.

Figure 6 shows the surface topography of the BaTiO<sub>3</sub> thin-films following conventional laser direct-write processing at  $\lambda=266$  nm. A SEM image of the as-received unexposed cubic BaTiO<sub>3</sub> thin-films is displayed in figure 6a and reveals that the native BaTiO<sub>3</sub> thin-films are relatively smooth and crack-free, highly crystalline and compositionally homogeneous. However, in the absence of laser genotype pulse “scripting” and position-synchronized photon delivery, laser-material energy coupling is inefficient under conventional laser direct-write irradiation at  $\lambda=266$  nm, and the phase conversion is sporadic and results in detrimental material processing effects –

including laser light scattering, variation in absorbed energy, enhanced energy confinement, non-uniform heating and residual stress and fracture.

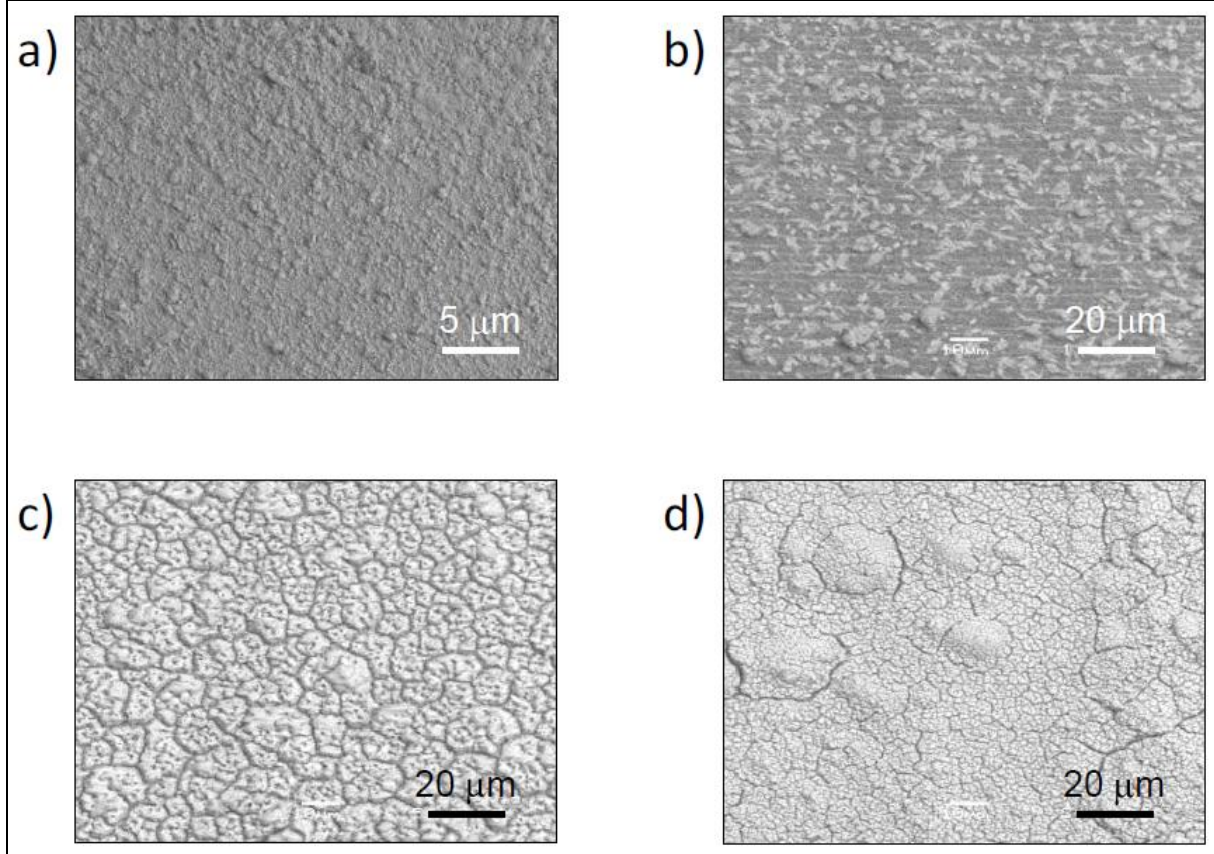


Figure 6. SEM images of  $\text{BaTiO}_3$  thin-films that were acquired (a) prior to laser exposure and (b)–(d) following conventional laser direct-write processing at  $\lambda=266$  nm.

Figure 6b shows a SEM image of the  $\text{BaTiO}_3$  thin-film surface following laser patterning at  $\lambda=266$  nm, where the average number of laser pulses administered to each spot was 30, the pulse repetition rate was 10 kHz, and the per-pulse fluence was set to  $6.0 \text{ J}\cdot\text{cm}^{-2}$ . The SEM results reveal a rough and highly corrugated surface morphology associated with significant material desorption and particulate ejection. Higher repetition rate and lower per-pulse fluence exposures were also employed, but caused similar damage to the  $\text{BaTiO}_3$  thin-films. Figures 6c and 6d display the SEM images acquired following 30 kHz laser irradiation at  $\lambda=266$  nm, where the average number of laser pulses delivered to each spot has been increased to 90 with per-pulse fluences of  $1.5 \text{ J}\cdot\text{cm}^{-2}$  and  $2.7 \text{ J}\cdot\text{cm}^{-2}$ , respectively. The SEM results again indicate marked surface disruption, which was manifested in particle sintering and aggregation, along with substantial film cracking and delamination.

The composite results shown in figures 4 and 5 strongly suggest that high fidelity laser pulse modulation and enhanced heating control are needed to promote pyroelectric phase conversion, while maintaining the overall integrity and mechanical stability of the  $\text{BaTiO}_3$  thin-films. Figure

6 displays a set of Raman spectra that were acquired following laser processing of 300-nm-thick BaTiO<sub>3</sub> thin-films using *genotype-inspired, digitally-scripted* laser direct-write techniques. The Raman results shown in figure 6 correspond to BaTiO<sub>3</sub> thin-films that were exposed to incident laser irradiation at  $\lambda=266$  nm (5 kHz; 520 fs pulse width) using the composite laser pulse scripts shown in the insets. The composite laser pulse scripts were synchronously delivered to each laser-irradiated spot during patterning, where the laser raster pattern corresponded to a 2 mm x 2 mm square with a sequential line fill, and a step-over between line scans that was equivalent to the laser spot size. The laser pulse scripts comprised high intensity, ultra short pulses at a low repetition rate with the following parameters: *Script 1*, 90 pulses, 1.5 J·cm<sup>-2</sup>; *Script 2*, 180 pulses, 1.6 J·cm<sup>-2</sup>; *Script 3*, 240 pulses, 3.1 J·cm<sup>-2</sup> (max). The laser-scripted processing results reveal that the pyroelectric phase transformation can be accomplished by the administration of a succession of laser pulses, i.e., inter-pulse conversion – where each pulse partially converts nano- and microscale domains of the BaTiO<sub>3</sub> thin-film from the cubic phase to the tetragonal phase. Metered laser exposure doses can, therefore, be used to induce sequential phase transformation, which will facilitate fine phase state control and laser-tuning of the electrical and pyroelectric properties of the BaTiO<sub>3</sub> thin-films. The enhanced conversion observed with pulse script 3 (which contained an initial “ramp” pulse profile) indicates that the laser pulse scripts must account for dynamic changes in the film’s properties, such as the refractive index, heat capacity and optical defect density; we are currently exploring these effects and their impact on the extent of laser-induced phase transformation.

The importance of laser pulse “scripting” and appropriately tailoring the photon flux to control heat flow in the BaTiO<sub>3</sub> crystal lattice is highlighted in figure 7, which compares the nanoscale surface topography before and after laser genotype processing at  $\lambda=355$  nm (80 MHz, 10 ps fwhm). Figure 8a displays an AFM image acquired prior to laser exposure (as-received), and corresponds to a relatively smooth BaTiO<sub>3</sub> thin-film with a nominal rms surface roughness of ~156 nm. Following laser-scripted exposure at  $\lambda=355$  nm (~1x10<sup>6</sup> pulses, per-pulse fluence= 3.6 mJ·cm<sup>-2</sup>), the AFM results reveal that the BaTiO<sub>3</sub> thin-film remains undisturbed with a comparable rms surface roughness of ~140 nm and no measurable material desorption or particulate ejection. This is in marked contrast to the substantial damage to the BaTiO<sub>3</sub> thin-film that was observed using conventional laser direct-write processing techniques (cf., figure 6).

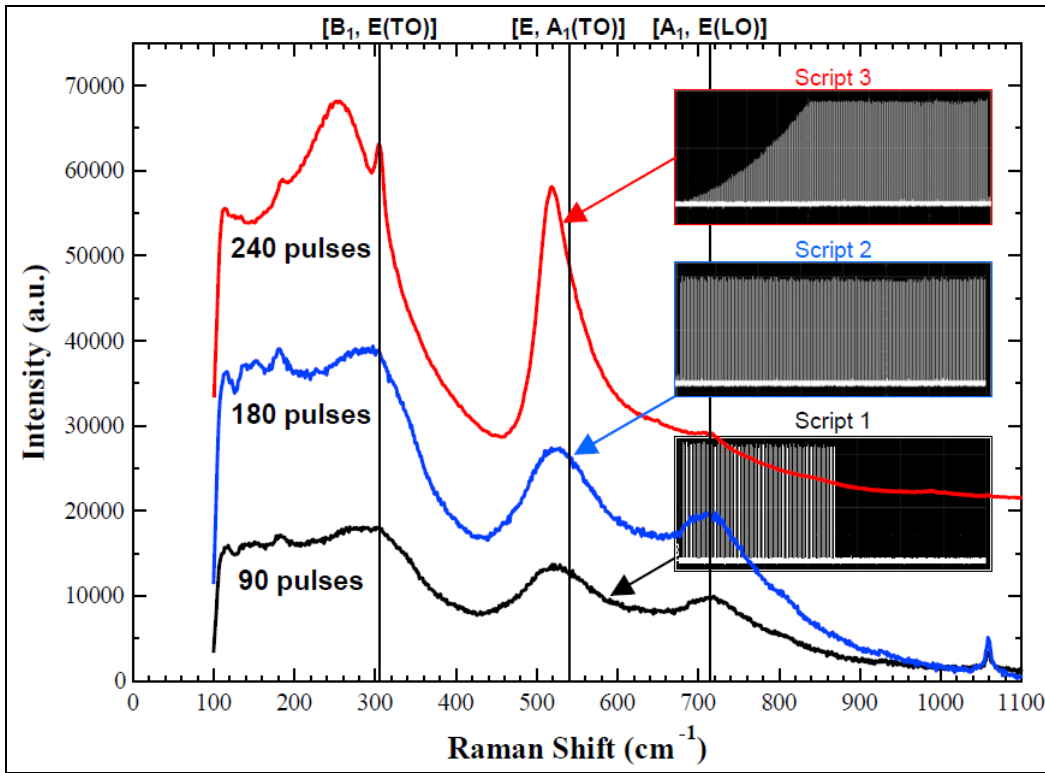


Figure 7. Raman spectra measured for  $\text{BaTiO}_3$  thin-films following digitally-scripted laser genotype direct-write processing at  $\lambda=266$  nm and 5 kHz. The laser pulse scripts corresponded to the following parameters: *script 1*, 90 pulses,  $1.5 \text{ J}\cdot\text{cm}^{-2}$ ; *script 2*, 180 pulses,  $1.6 \text{ J}\cdot\text{cm}^{-2}$ ; *script 3*, 240 pulses,  $3.1 \text{ J}\cdot\text{cm}^{-2}$  (max).

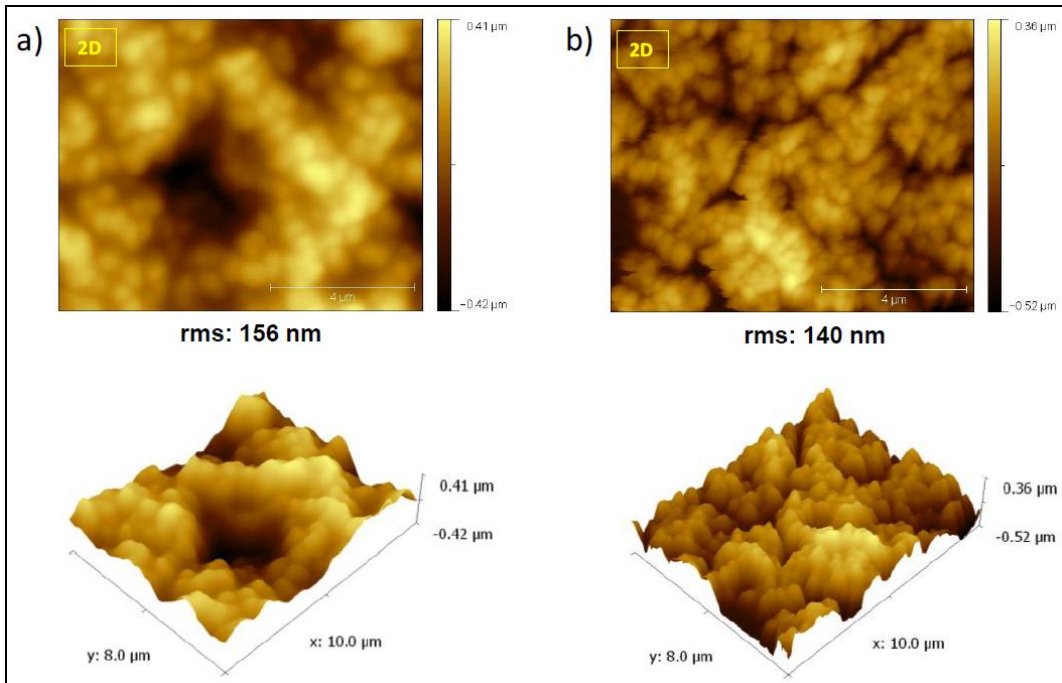


Figure 8. AFM images of BaTiO<sub>3</sub> thin-films that were acquired (a) prior to laser exposure and (b) following digitally-scripted laser genotype direct-write processing and pyroelectric phase conversion at  $\lambda=355$  nm. Note that the perovskite film remains unperturbed during the laser-induced phase transformation process when laser pulse “scripting” is employed for high fidelity heat control.

### 3. Progress by the Institute for Collaborative Biotechnologies (ICB)

#### 3.1 T<sub>c</sub> with Ba<sub>1-x</sub>Sr<sub>x</sub>TiO<sub>3</sub>; Doping with CeO<sub>2</sub>; Preparation of Thicker Films

ICB prepared and provided our Aerospace and ARL partners films composed of oleic acid functionalized Ba<sub>1-x</sub>Sr<sub>x</sub>TiO<sub>3</sub> (BSTO) and CeO<sub>2</sub>-doped BSTO nanoparticles synthesized by vapor diffusion catalysis from Ba/Ti- and Sr/Ti bimetallic alkoxide precursors with or without addition of a cerium alkoxide precursor (figures 9, 11, and 12). We found that this method enables us to precisely tune the electric properties of the final ceramics (e.g., the phase transition temperature) through carefully adjusting the Ba:Sr ratio by appropriate control of the mixture of the precursor materials. Electrical characterization after annealing showed that the nanopowder consisting of 15% Sr and 85% Ba (metal content was determined by ICP) exhibits a significant decrease in the Curie temperature (T<sub>c</sub>) from the 120 °C, characteristic of bulk BaTiO<sub>3</sub>, to ~80 °C (figure 10). We and our partners, therefore, chose BSTO as a model system for further investigation because it has several desirable properties for both IR detector and laser processing applications. These include a relatively large dielectric constant, good pyroelectric response near room temperature, low dielectric loss and leakage current, and phase transition temperature controllable by the amount of Sr incorporated.

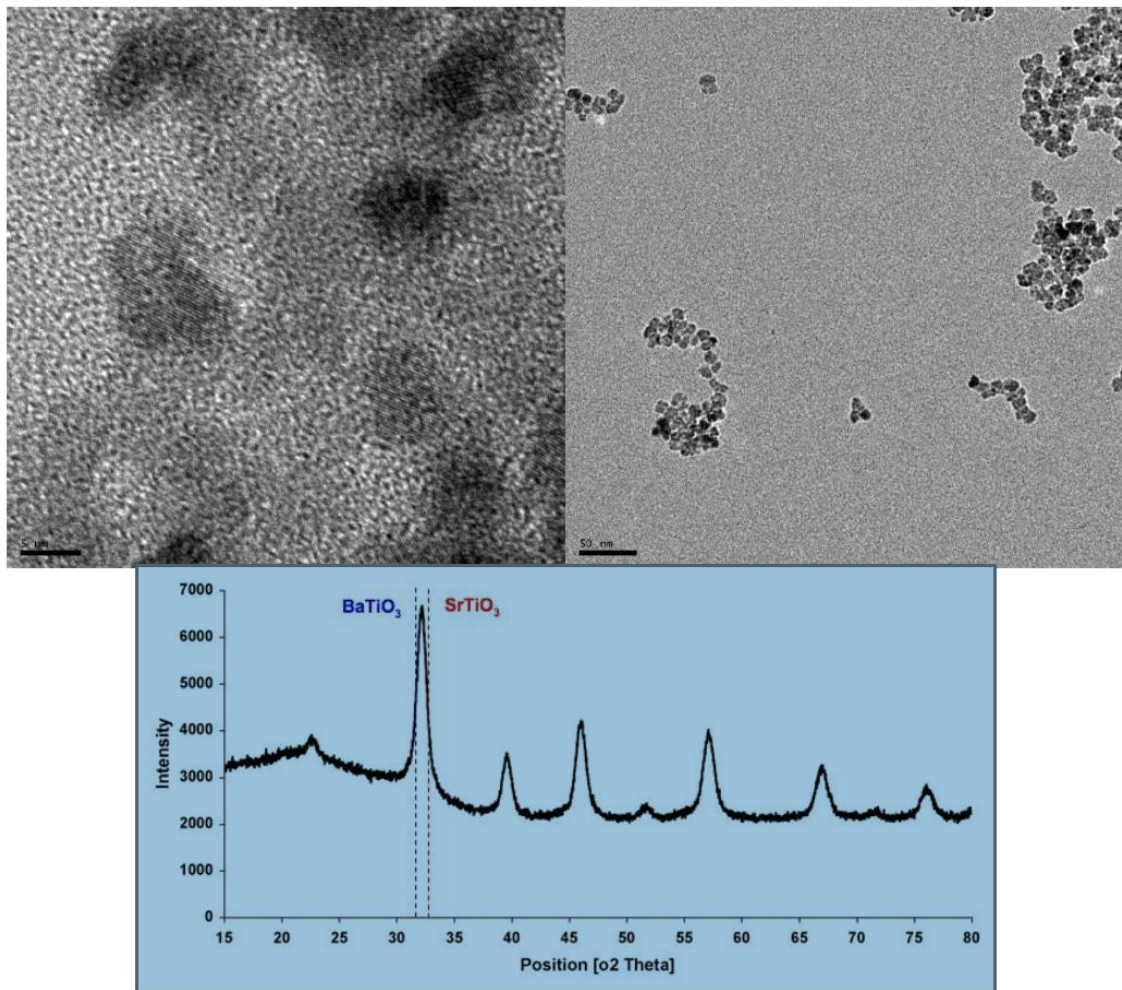


Figure 9. TEM and XRD analyses of BSTO nanoparticles prepared by vapor diffusion catalytic synthesis. Dotted lines on the XRD curve show the positions of the (110) reflections in pure bulk BaTiO<sub>3</sub> and SrTiO<sub>3</sub>, respectively.

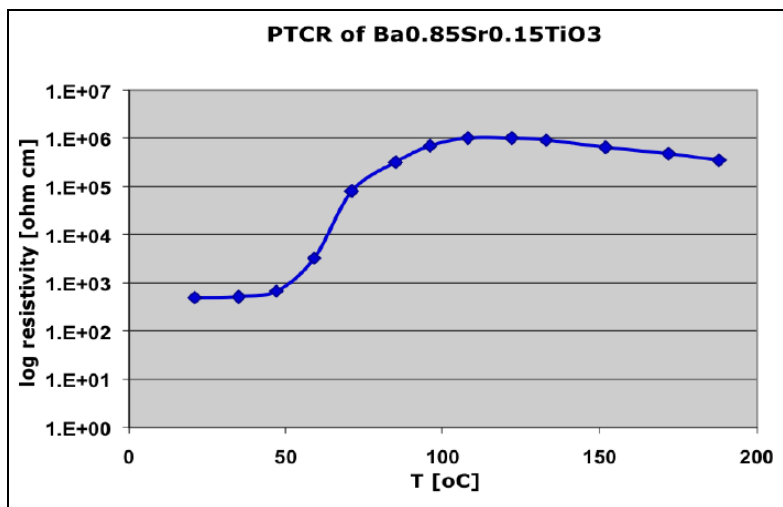


Figure 10. PTCR (positive thermal coefficient of resistivity) of the sintered BSTO ceramic, showing a reduced Curie temperature of ca. 80 °C.

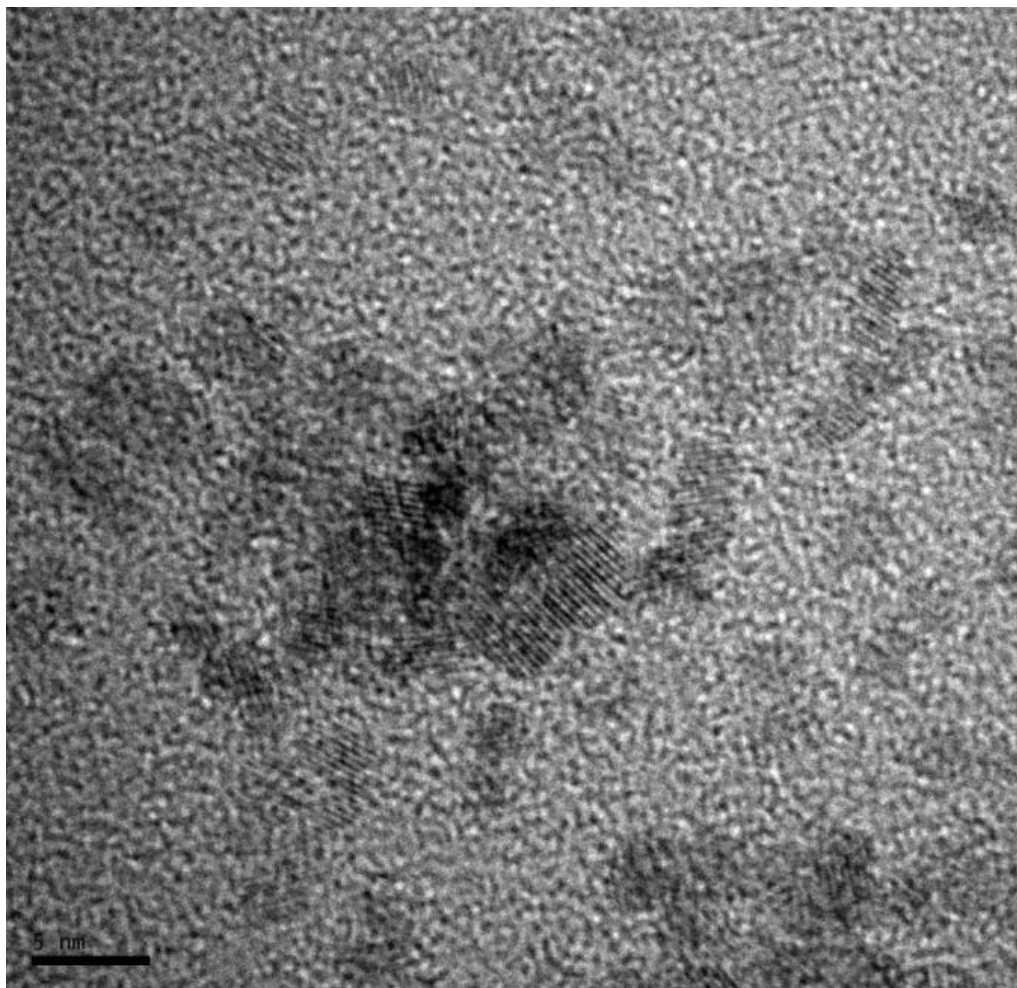


Figure 11. TEM image of CeO<sub>2</sub> nanoparticles prepared by vapor diffusion catalytic synthesis.

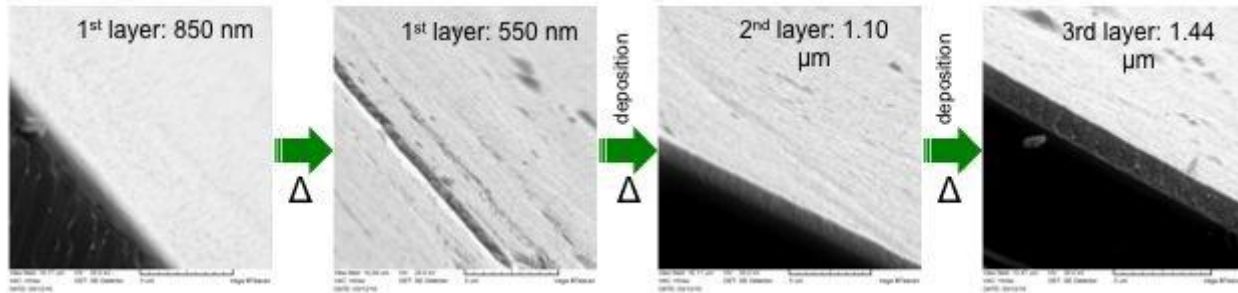


Figure 12. SEM images of the high-quality doped BSTO films produced by layer-by-layer deposition followed by annealing.

To increase the throughput and efficiency of laser-induced phase transformation in the thin-films (~210 nm thick, with potentially fast response time), nanoparticulate  $\text{CeO}_2$  exhibiting high photon absorption in the UV range was incorporated into the nanopowder prior to film deposition. For this purpose, we used a method we recently reported for the synthesis of 3.5 nm ceria nanoparticles from alkoxide precursors under conditions similar to those used for BTO or BSTO nanoparticle synthesis (figure 11), thereby promoting the formation of the two oxide materials simultaneously.

To produce this composite film, the appropriate amounts of Ba/Ti- and Sr/Ti bimetallic alkoxides were mixed in the precursor solution (to yield  $\text{Ba}_{1-x}\text{Sr}_x\text{TiO}_3$ ,  $x = 0.15$ ) with the addition of cerium isopropoxide ( $\text{Ce}(\text{OC}_3\text{H}_7)_4$ ) prior to hydrolysis and polycondensation. The targeted  $\text{CeO}_2$  concentration in the resulting solid nanopowder was 0.03 wt%. After collection of the resulting nanoparticle composite, oleic acid was added in hexane followed by sonication to functionalize the surface of the nanoparticles. After precipitation and intensive washing, the solid powder was finally re-dissolved in non-polar solvents (e.g., hexane, toluene), in which it remained stable for days. The colloid nanocrystals were then subjected to layer-by-layer deposition through spin coating to make thicker films for better pyroelectric response. Each deposition step was followed by a subsequent annealing cycle at 300 °C to remove hydrocarbons and to densify the films. Previous results showed that thick films (~5 μm) cracked when heated to 300 °C as a result of the gas evolution during annealing. We successfully circumvented that problem in this case by depositing the doped BSTO in thinner layers, with heating and cooling cycles performed at very low ramping rates (2 °C/min) to avoid cracking. SEM characterization shows that the films not only survived the annealing steps, but there was a significant densification due to particle rearrangement and the removal of the residual organics (figure 12). Thickness of the first film thus changed from the initial value of 850 nm to 550 nm after annealing at 300 °C for 2 hr; each additional layer, after annealing, produced a further significant increase in film thickness without the introduction of cracks. Thus, the thickness after deposition of the 2nd layer was 1.10 μm, and after deposition of the 3rd layer, 1.44 μm.

### 3.2 Further Progress in Scale-Up and Delivery to Quallion

**a. Routine production doubled again:** Using the mid-scale reactor design shown in our previous reports, we now have increased routine production of 7 nm BaTiO<sub>3</sub> and Ba<sub>1-x</sub>Sr<sub>x</sub>TiO<sub>3</sub> nanoparticles to 250 g/batch (a doubling from our previous routine production of 100g/batch). Characterization by XRD, XPS, and TEM shows the product to be the same high quality and purity crystalline material as previously reported, with quantitative yield. Results are reported in a manuscript submitted to *Nature Protocols*.

**b. Progress toward continuous production:** Progress on the construction of a large-scale reactor is nearing completion. This will enable trials of continuous-flow production with automated controls. This reactor incorporates several changes in design to increase throughput, including the use of nebulizers to deliver the reactants as a fine mist of micro-droplets, thereby accelerating diffusion and the resulting reaction kinetics governing synthesis. Preliminary trials of the apparatus operated with manual control produced pure, highly crystalline nanoparticles of BaTiO<sub>3</sub> with no contaminants detectable.

**c. Increase in throughput with sonication-accelerated synthesis:** Sonication is being optimized experimentally, in an effort parallel to that described above, to increase the speed throughput of synthesis. Results show considerable promise:

*We found that ultrasonication significantly accelerates the quantitative conversion of the bimetallic alkoxide precursor to the highly crystalline final perovskite (BaTiO<sub>3</sub>) in only 3 h, representing a significantly increased throughput compared to previous results using vapor diffusion catalysis alone (typically requiring 2 days for completion of the process. (The high quality, quantitative yield and purity of the product were confirmed by XRD, XPS, TEM, Raman spectroscopy, and DTA analyses.)*

Our experimental analyses allow us to conclude that major factors responsible for the dramatically increased crystallization rates observed in the sonication-assisted syntheses can be attributed to the enhanced transport of water/acid catalyst molecules into the metal alkoxide precursors, the increased mixing rate of the alkoxide and water molecules and the accelerated formation of nucleation centers on the cavitation bubbles. Agitation of the precursor solutions through high-intensity sonication facilitates the formation of high surface areas of the liquid precursors, enhancing contact with the acidic water mixture, the transport of which is greatly increased either through an increase in evaporation rate or the formation of micro-droplets by sonication. The enhanced diffusion rate of water and acid molecules results in faster mixing of the reaction components. Finally, the increased crystallization rate, a significant and well-known effect of sonication, also is likely to contribute to the accelerated synthesis of the oxide nanoparticles. It also is possible that, as a consequence of the collapse of high-energy cavitation bubbles, the evaporation rate of solvent from the precursor solution is increased as well, further contributing to the shortened diffusion path for the water molecules. Furthermore, we have observed a mist of micro-droplets generated from the precursor solution above the liquid level,

and solid product floating on the liquid surface within only half an hour after the start of sonication. This observation suggests the formation of small droplets with high surface area and high surface energy during the initial stages of product growth. These microscopic aerosol pools contain the reactive precursor, which can interact instantly with the aqueous catalyst through droplet collision, producing small oxide and perovskite nanoparticles. This mechanism is the subject of our ongoing investigation, focusing on the droplet size dependency, controlled by sonication in the MHz frequency regime, of the size of nanocrystals produced, and the possibility of making this process continuous.

These results are reported in a manuscript now in press in *Nano Today*.

Further improvements are now under investigation using tunable megahertz ultrasonication of both the precursor and catalyst.

---

## 4. Progress by the Army Research Laboratory (ARL)

---

### 4.1 Sacrificial Layer Deposition; Electrical Characterization; Nanostructured IR Absorbing Layer Development

#### 4.1.1 Sacrificial Layer Deposition

In order to achieve low thermal mass, the proposed final structure includes a suspended MEMs membrane (figure 13). We must be able to release the BaTiO<sub>3</sub> film from the substrate without damaging the film.

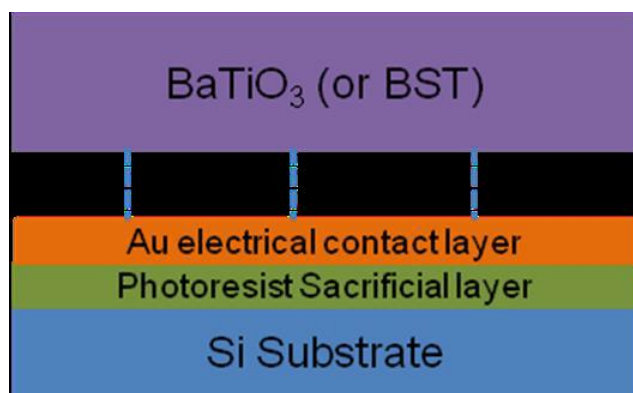


Figure 13. IR test heterostructure.

We began investigating potential release layers. We began by spin-coating PMMA, which is an inexpensive, transparent thermoplastic commonly used as photoresist in electron beam lithography. The next step was to evaporate Pt onto the PMMA layer (to serve as the bottom electrical contact). The Pt did not adhere to the PMMA.

We then attempted to use AZ-5214E, which is a photoresist intended for lift-off techniques. We were able to evaporate a well-adhering bottom metal electrode layer or BST layer deposition. Ultimately, AZ-5214E will not work in the final structure, since it cannot be exposed to temperatures above 120 °C. The current structure will serve as a practice tool for lifting off and handling the membrane and for studying its physical properties.

#### 4.1.2 Electrical Characterization

The laser-activated tetragonal BaTiO<sub>3</sub> pixels must be electrically isolated from one another. We wire bonded a structure, as shown in figure 14, for the purpose of capacitance measurements. After numerous attempts, we are finding that all structures that include the top metal layer are electrical shorts. By using epoxy to attach wires to a film that did not have a top metal contact, we found the film to be electrically resistive, as expected. XPS studies are in progress to determine if the top or bottom electrode layer is diffusing into the BaTiO<sub>3</sub> film. Another potential source for electrical shorting would be metal traveling through micropores in the film, although earlier SEM did not indicate that this is likely.

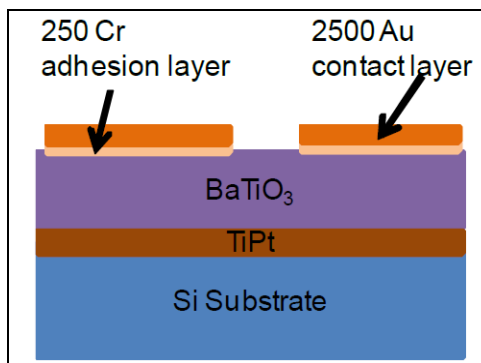


Figure 14. Wire bonding for capacitance measurements.

#### 4.1.3 Nanostructured IR Absorbing Layer Development

Thermal detectors require a layer similar to a thin coating of black paint that absorbs a wide range of wavelengths and heats up. The heat is transferred to the BT layer and the pyroelectric voltage is generated. We are developing a low cost technique that is temperature-compatible with the bio-inspired BaTiO<sub>3</sub> films and with ROIC technology.

We have grown a series of multilayer films comprising silicon/gold-nanoparticles and silicon/silicon dioxide/gold-nanoparticles to determine the required heat treatment (to form the nanoparticles) and etch parameters (to create the nanostructures in the surface of the film) required to make the film strongly absorbing in the 3 to 12 micron wavelength band. A schematic of the structure is shown in figure 15. The films are characterized using AFM, SEM and Fourier transform infrared spectroscopy. Figure 16 shows the particle formation after the heating but before the etch process.

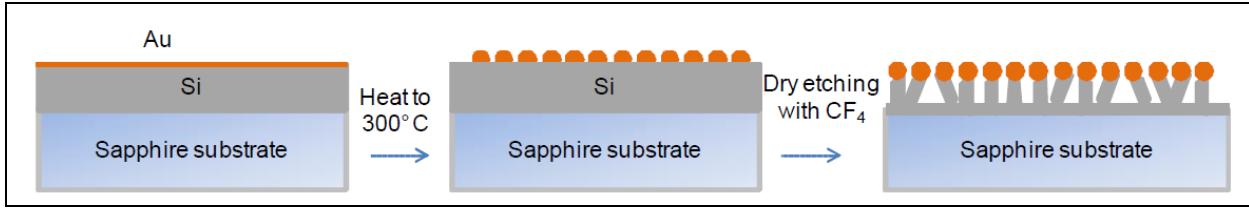


Figure 15. Processing steps required for the generation of nanostructured Si pillars for enhanced IR absorption.

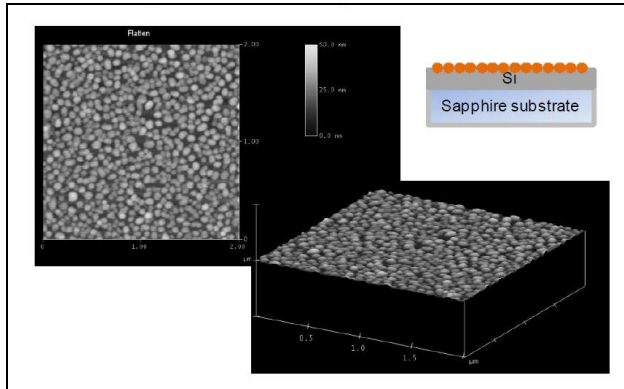


Figure 16. AFM images of Au particle formation prior to etching.

#### 4.2 Update of Proposed Processing Steps

After the second year review, it became clear that a comparison of our processing steps with conventional methods was needed. We updated our proposed processing steps to incorporate changes from our original proposal.

The standard optical lithography pixel delineation process includes:

- spinning a liquid photoresist onto the wafer
- baking the wafer for about an hour, exposing the wafer (the mask could have several arrays on it depending on the size)
- developing the resist (minutes), rinse and dry, then any etching or deposition required
- for a complicated structure, a wafer will go through the photolithographic steps (a-c) several times (~50 times).

Figure 17 shows a film grown by conventional MBE with pixels formed by photolithography, followed by substrate thinning, IR absorbing layer deposition, and flip-chip bonding to a fan-out or ROIC.

Figure 18 shows a similar process using laser-induced pyroelectric activation and bump bonding to a Si fan-out. This procedure will be used to prove proof-of-principle. These steps, made possible by low-temperature growth and site-specific laser processing, are not reliant on photolithography or flip-chip bonding, and there is no substrate thinning step.

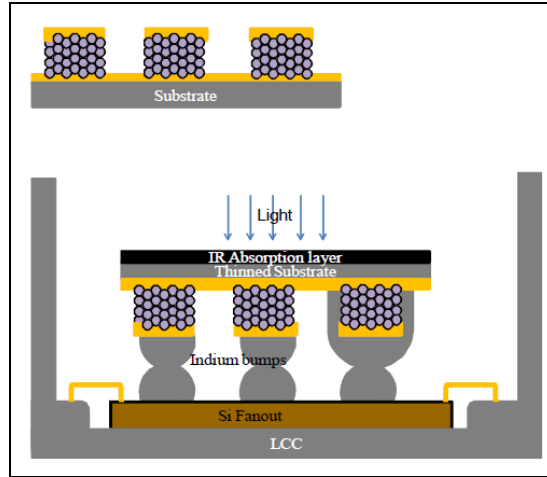


Figure 17. Pixel formation accomplished via conventional approaches.

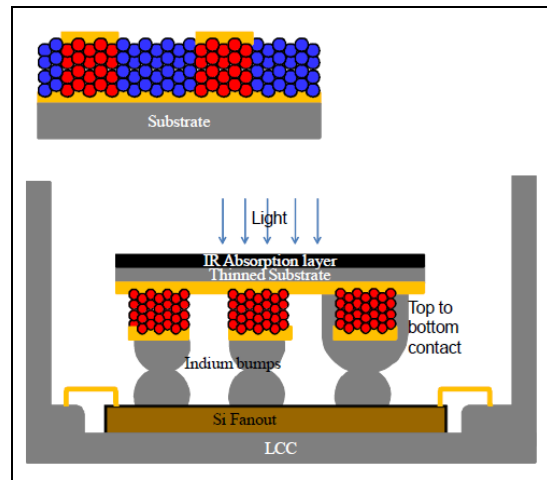


Figure 18. Pixel formation accomplished via laser-induced pyroelectric activation.

---

## 5. Plans and Goals for Year 2 Quarter 4

---

In the coming quarter, we will continue to expand our nanomaterial synthesis capabilities, laser processing techniques and spectroscopic phase conversion studies, and perovskite thin-film electrical characterization efforts. We also intend to initiate and pursue several new areas of focus: *ICB*: finalize construction of the large-scale reactor and pursue trials of continuous-flow production with automated control, and further investigate accelerated synthesis and improved throughput of pure and CeO<sub>2</sub>-doped BaTiO<sub>3</sub> and BaSrTiO<sub>3</sub> nanoparticles using MHz ultrasonication methods; *Aerospace*: conduct laser-scripted processing studies on the newly synthesized BaSrTiO<sub>3</sub> and CeO<sub>2</sub>-doped nanoparticle thin-films, investigate the optical

spectroscopy and photoemission characteristics of these novel material systems for optimized pyroelectric activation and process control, and explore the use of the IR absorbing layer for heating and patterned pyroelectric phase conversion of the underlying perovskite thin-film; *ARL*: perform electrical characterization and temperature-dependent pyroelectric measurements on ICB-provided functionalized BaTiO<sub>3</sub> thin-films, and investigate the use of black silicon nanopillar structural layers for enhanced IR absorption.

---

## 6 Metrics for Year 2 Quarters 2 and 3

---

### 6.1 Publications

1. Ould-Ely, T.; Niesz, K.; Luger, M.; Doherty, M.; Morse, D. E. First Large-scale Engineered Synthesis of BaTiO<sub>3</sub> Nanoparticles Using Low Temperature Bioinspired Principles. *Nature Protocols* **2010**, submitted.
2. Livingston, F. E.; Sarney, W. L.; Little, J. W.; Olver, K. A.; Niesz, K.; Morse, D. E. Laser-induced Structuring of Bio-inspired Nanomaterials for Sensor Technology Applications, Proceedings of the Military Sensing Symposium. *Joint Session on Materials/Detectors: Uncooled IR Detector and FPA Technology*, Orlando, FL, Feb. 23, 2010.
3. Niesz, K.; Morse, D. E. Sonication-accelerated Catalytic Synthesis of Oxide Nanoparticles. *Nano Today* **April 2010**, 5 (2), 99–105.
4. Livingston, F. E.; Helvajian, H. Laser Processing Architecture for Improved Material Processing. in *Laser Processing of Materials: Fundamentals, Applications, and Developments*, P. Schaaf, Ed., Springer Series Materials Science, **2010**, invited book chapter in press.
5. Sarney, W. L.; Little, J. W.; Livingston, F. E.; Niesz, K.; Cole, M. W.; Morse, D. E. Low Temperature Growth and Laser-induced Phase Transformation of Perovskite Oxide Films for Uncooled IR Detector Applications. *Mater. Res. Soc. Symp. Proc.* **2010**, 1199.

### 6.2 Conferences and Symposia

1. Livingston, F. E.; Sarney, W. L.; Niesz, K.; Morse, D. E. Laser Direct-write Activation of Perovskite Nanoparticle Films for Thermal Detector Applications, National Defense Industrial Association (NDIA) – *11th Annual Science & Engineering Technology Conference/DoD Tech. Exposition*, abstract accepted for presentation in Orlando, FL, Apr. 2010.

2. Livingston, F. E.; Sarney, W. L.; Niesz, K.; Little, J. W.; Olver, K. A.; Morse, D. E. Laser Tailoring of Bio-inspired Thin-films for Improved Sensitivity, Low-cost Uncooled IR Detector FPAs, *2010 Institute for Collaborative Biotechnologies (ICB) Army-Industry Collaboration Conference*, UC Santa Barbara, CA, Mar. 3–4, 2010.
3. Livingston, F. E.; Sarney, W. L.; Little, J. W.; Olver, K. A.; Niesz, K.; Morse, D. E. Laser-Induced Structuring of Bio-inspired Nanomaterials for Sensor Technology Applications. invited talk at the *Military Sensing Symposia (MSS) – Joint Session on Materials/Detectors: Uncooled IR Detector and FPA Technology*, Orlando, FL, Feb. 23, 2010.
4. Sarney, W. L.; Little, J. W.; Livingston, F. E.; Niesz, K.; Morse, D. E. Pyroelectric films Synthesized by Low-temperatures and Laser-processed for Uncooled Infrared Detector Applications. *International Semiconductor Device Research Symposium*, College Park, MD, Dec. 9, 2009.
5. Sarney, W. L.; Little, J. W.; Livingston, F. E.; Niesz, K.; Cole, M. W.; Morse, D. E. Low Temperature Growth and Laser-induced Phase Transformation of Perovskite Oxide Films for Uncooled IR Detector Applications. *Materials Research Society Fall Meeting*, Boston, MA, Dec. 4, 2009.

---

## 7. References

---

1. Sarney, Wendy L. et al. *Improved Sensitivity Low-cost Uncooled Infrared (IR) Detector Focal Plane Arrays*; ARL-TR-4721; U.S. Army Research Laboratory: Adelphi, MD, February 2009.
2. Sarney, Wendy L. et al. *Progress in Biologically Inspired Pyroelectric Materials Growth for Improved Sensitivity, Lower-cost Uncooled IR Detector Focal Plane Arrays*; ARL-TR-4770; U.S. Army Research Laboratory: Adelphi, MD, April 2009.
3. Sarney, Wendy L. et al. *Bio-inspired Materials Research for Improved Sensitivity Low-cost Uncooled Infrared (IR) Detector Focal-plane arrays*; ARL-TR-5172; U.S. Army Research Laboratory: Adelphi, MD, April 2010
4. Sarney, Wendy L. et al. *Further Developments in Improved Sensitivity, Low-cost Uncooled IR Detector Focal Plane Arrays*; ARL-TR-5389; U.S. Army Research Laboratory: Adelphi, MD, November 2010.
5. Wemple, S. H. *Phys. Rev. B* **1970**, 2, 2679.
6. Xu, J.; Durisin, D. P.; Auner, G. W. *Proc. SPIE* **2005**, 5713, 305.
7. Matsuda, H.; Kobayashi, N.; Kobayashi, T.; Miyazawa, K.; Kuwabara, M. *J. Non-Cryst. Solids* **2000**, 271, 162.
8. Kamalasan, M. N.; Chandra, S.; Joshi, P. C.; Mansingh, A. *Appl. Phys. Lett.* **1991**, 59, 3547.
9. Harizanov, O.; Harizanova, A.; Ivanova, T. *Mater. Sci. Engineer.* **2004**, B106, 191.
10. Golego, N.; Studenikin, S. A.; Cocivera, M. *Chem. Mater.* **1998**, 10, 2000.
11. Guo, H.; Liu, L.; Chen, Z.; Ding, S.; Lu, H.; Jin, K.-J.; Zhou, Y.; Cheng, B. *Europhys. Lett.* **2006**, 73, 110.

---

## **List of Symbols, Abbreviations, and Acronyms**

---

AFM	atomic force microscopy
ARL	U.S. Army Research Laboratory
BaTiO <sub>3</sub>	barium titanium oxide
BST	barium strontium titanate
ICB	Institute for Collaborative Biotechnologies
IR	infrared
MBE	molecular beam epitaxy
nm	nanometer
PCD	pulsed laser deposition
PFM	piezoelectric force microscopy
PMMA	polymethyl methacrylate
SEM	scanning electron microscope
SHG	second harmonic generation
Si	silicon
UV	ultraviolet
XRD	x-ray diffraction
Y2Q2/3	year two, quarters two and three

NO. OF COPIES	ORGANIZATION	NO. OF COPIES	ORGANIZATION
1	ADMNSTR	1	THE AEROSPACE CORPORATION
ELEC	DEFNS TECHL INFO CTR		MICRO/NANOTECHNOLOGY
	ATTN DTIC OCP		DEPARTMENT
	8725 JOHN J KINGMAN RD STE 0944		SPACE MATERIALS LABORATORY
	FT BELVOIR VA 22060-6218		ATTN F LIVINGSTON
			2350 E EL SEGUNDO BLVD
1 CD	OFC OF THE SECY OF DEFNS		EL SEGUNDO CA 90245
	ATTN ODDRE (R&AT)		
	THE PENTAGON	6	US ARMY RSRCH LAB
	WASHINGTON DC 20301-3080		ATTN IMNE ALC HRR
1	US ARMY RSRCH DEV AND ENGRG		MAIL & RECORDS MGMT
	CMND		ATTN RDRL CIO LL TECHL LIB
	ARMAMENT RSRCH DEV & ENGRG		ATTN RDRL CIO MT TECHL PUB
	CTR		ATTN RDRL SEE I K OLVER
	ARMAMENT ENGRG & TECHNLGY		ATTN RDRL SEE I W SARNEY
	CTR		ATTN RDRL SEE O J WHITE
	ATTN AMSRD AAR AEF T		ADELPHI MD 20783-1197
	J MATTS		
	BLDG 305		
	ABERDEEN PROVING GROUND MD		
	21005-5001		
1	PM TIMS, PROFILER (MMS-P)		
	AN/TMQ-52		
	ATTN B GRIFFIES		
	BUILDING 563		
	FT MONMOUTH NJ 07703		
1	US ARMY INFO SYS ENGRG CMND		
	ATTN AMSEL IE TD A RIVERA		
	FT HUACHUCA AZ 85613-5300		
1	COMMANDER		
	US ARMY RDECOM		
	ATTN AMSRD AMR		
	W C MCCORKLE		
	5400 FOWLER RD		
	REDSTONE ARSENAL AL 35898-5000		
1	US GOVERNMENT PRINT OFF		
	DEPOSITORY RECEIVING SECTION		
	ATTN MAIL STOP IDAD J TATE		
	732 NORTH CAPITOL ST NW		
	WASHINGTON DC 20402		
2	INSTITUTE FOR COLLABORATIVE		
	BIOTECHNOLOGIES UNIVERSITY		
	OF CALIFORNIA, SANTA BARBARA		
	ATTN D MORSE		
	ATTN K NIESZ		
	SANTA BARBARA CA 93106-5100		

INTENTIONALLY LEFT BLANK.